HHS Public Access

Author manuscript

J Am Chem Soc. Author manuscript; available in PMC 2024 June 07.

Published in final edited form as:

J Am Chem Soc. 2024 January 10; 146(1): 500–513. doi:10.1021/jacs.3c09983.

Modulation of the Bonding between Copper and a Redox Active Ligand by Hydrogen Bonds and its Effect on Electronic Coupling and Spin States

Dolores L. Ross[†], **Andrew J. Jasniewski**[§], **Joseph W. Ziller**[†], **Emile L. Bominaar**[⊥], **Michael P. Hendrich**[⊥], **A.S. Borovik**[†]

[†]Department of Chemistry, 1102 Natural Science II, University of California, Irvine, CA 92697 USA

[§]Department of Molecular Biology and Biochemistry, University of California, Irvine, CA 92697 USA

[⊥]Department of Chemistry, Carnegie Mellon University, Pittsburgh, PA 15213 USA

Abstract

The exchange coupling of electron spins can strongly influence the properties of chemical species. The regulation of this type of electronic coupling has been explored within complexes that have multiple metal ions but to a lesser extent in complexes that pair a redox-active ligand with a single metal ion. To bridge this gap, we investigated the interplay among the structural and magnetic properties of mononuclear Cu complexes and exchange coupling between a Cu center and a redox-active ligand over three oxidation states. The computational analysis of the structural properties established a relationship between the complexes' magnetic properties and a bonding interaction involving a $d_{x^2-y^2}$ orbital of the Cu ion and π orbital of the redox-active ligand that are close in energy. The additional bonding interaction affects the geometry around the Cu center and was found to be influenced by intramolecular H-bonds introduced by the external ligands. The ability to synthetically tune the d-π interactions using H-bonds illustrates a new type of control over the structural and magnetic properties of metal complexes.

Graphical Abstract

Corresponding Authors: eb7g@andrew.cmu.edu, hendrich@andrew.cmu.edu, aborovik@uci.edu.

ASSOCIATED CONTENT

Supporting Information

The Supporting Information is available free of charge on the ACS Publication website at DOI: The following file is available free of charge.

Experimental and theoretical descriptions and characterization data for all new compounds, Tables S1–S11, Figures S1–S46, and details for the molecular structures from XRD methods in cif format.

Accession Codes

CCDC 2291041–2291043 contain the supplementary crystallographic data for this paper. These data can be obtained free of charge via www.ccdc.cam.ac.uk/data_request/cif, or by emailing data_request@ccdc.cam.ac.uk, or by contacting The Cambridge Crystallographic Data Centre, 12 Union Road, Cambridge CB2 1EZ, UK; fax: +44 1223 336033.

Notes

The authors declare no competing financial interests.

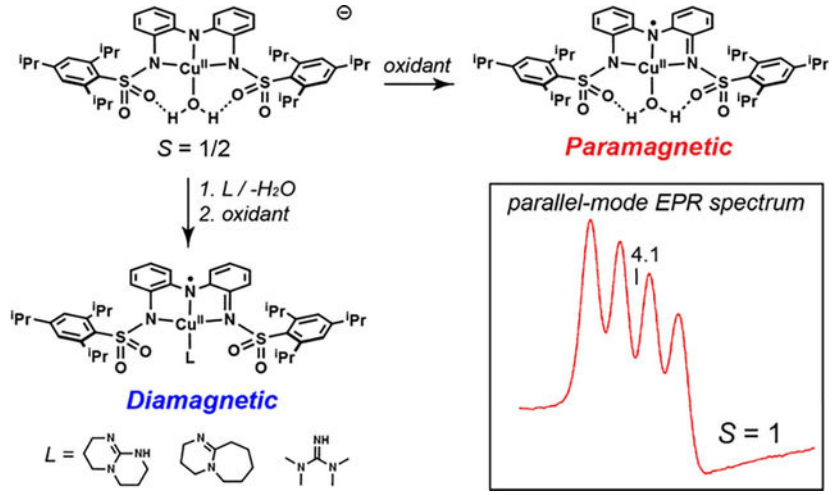

Introduction

Multi-electron processes are prevalent in thermodynamically challenging chemical transformations.[1–3] Synthetically, these processes commonly use complexes containing second- and third-row metal ions to supply the necessary redox equivalents. The thermodynamic limitations of first-row metal ions hinder their usage in these types of reactions; however, their natural abundance makes them more accessible than precious metals, and efforts to prepare complexes containing first-row metal ions that can provide reactivity comparable to that of precious metal complexes have been underway for several decades. To overcome the constraints of first-row metal ions, two routes are often utilized: multiple metal ions can be included in the catalytically competent species, or an alternative source of redox equivalents can be supplied through the coordination of a redox-active ligand.[4,5] This class of ligands has been employed with notable successes in a variety of metal complexes and is recognized to produce systems with unusual electronic and functional properties (Figure 1A–D).[6–19] A key feature of these systems is the occurrence of electronic coupling between the metal center and the redox-active ligand, which potentially provides a means of regulating the physical and functional properties of the complexes.

Pincer-type ligands, including those with multiple N-atom donors (denoted [NNN]), are often used as redox sources.[20] Heyduk has shown the utility of redox-active ligands in establishing reactivity towards small molecules. This utility is demonstrated by a Ta(V) complex that, despite being d^0, exhibits reactivity that is attributed solely to the [NNN] redox-active ligand (Figure 1A).[6,21] Work by Bröring and Tomat shows that the tripyrrindione ligand precursor hexaethyltripyrrin-1,14-dione (H_3TD1) coordinates to Cu^{II} centers as a radical dianion in the one-electron-oxidized form, which can supply an additional electron (Figure 1B).[7,8] The primary coordination sphere of the Cu^{II} center is completed by an aqua ligand that forms two intramolecular hydrogen bonds (H-bonds) with the $[TD1\cdot]^{2-}$ ligand. Despite H-bonds being noncovalent interactions, they have been shown to impact the structure and function of many systems.[22–27] This secondary coordination sphere motif demonstrated by the $[TD1\cdot]^{2-}$ ligand is also applied in related systems by Garcia-Bosch, where a diurea pincer ligand interacts with either a hydroxido or aqua ligand

within a Cu–OH_x system (Figure 1C); reactivity toward phenols was found for the oxidized Cu–OH species in which the oxidative equivalents were stored within the redox-active ligand framework.[9] Similarly, a four-coordinate redox-active ligand from Storr and Thomas that can store two oxidizing equivalents has been used to prepare Cu complexes that exhibit reactivity toward organic substrates (Figure 1D).[10]

The presence of multiple sites capable of redox chemistry within a single molecule affords the possibility of intramolecular exchange coupling of the electron spins. This coupling can influence the properties of the molecule, including its overall spin state, in ways unattainable by molecules containing a single redox site. Previous investigations have compared the magnetic properties of related compounds containing redox-active ligands,[28–32] but the modulation of exchange coupling by varying an ancillary ligand has been understudied in synthetic systems. This type of modulation is observed in heme proteins, which contain an axially coordinated ligand that directs the mode of electronic coupling between the metal ion and redox-active porphyrin. For example, within high-valent Fe–oxido intermediates in heme enzymes, the axial thiolate of the mono-oxygenases cytochrome P450s (P450s) imparts the active intermediate (compound I) with an $S = 1/2$ spin ground state via antiferromagnetic coupling between the Fe^{IV} center ($S = 1$) and porphyrin cation radical,[33] whereas the tyrosinate axial ligand of heme catalases enforces ferromagnetic coupling and therefore an $S = 3/2$ spin ground state.[34]

To explore whether exchange coupling can similarly be controlled within synthetic non-heme complexes, we have investigated the magnetic properties of Cu^{II} complexes with the redox-active ligand *N,N'*-(azanediyly-bis(2,1-phenylene))bis(2,4,6-triisopropyl-benzene-sulfonamido) ($[ibaps]^{3-}$, Figure 1E) having a series of ancillary ligands (Figures 1F & 1G). We previously demonstrated that Fe, Ga, and Ni complexes of $[ibaps]^{3-}$ have rich electrochemical properties and that the sulfonamido groups can be H-bond acceptors to promote intramolecular H-bond formation.[35,36] Examination of the redox and structural properties of the Cu complexes reported here allowed us to monitor differences in the electronic structure with four different ancillary ligands that have 0, 1, or 2 H-bond donors over three oxidation levels. Owing to the similar energies of the $d_{x^2-y^2}$ orbital of the Cu^{II} center and the redox-active π orbital of $[ibaps]^{3-}$, a nascent bond forms between a tilted $d_{x^2-y^2}$ orbital and the p_z orbital of the central N atom of $[ibaps]^{3-}$, which we discovered promotes molecular distortions away from the customary square planarity of four-coordinate Cu^{II} complexes. These distortions and their effect on the electronic properties of the complexes are shown to correlate with the spin state of the 1e-oxidized complexes. Our findings further illustrate the influence of intramolecular H-bonds on molecular structures and their applicability in regulating the magnetic properties of metal complexes.

The molecular distortions observed in the series of Cu complexes are also shown to correlate with the experimental hyperfine splittings of Cu^{II}. The hyperfine interactions in Cu^{II} complexes are commonly probed with electron paramagnetic resonance (EPR) spectroscopy, and the spectra typically show resolved hyperfine splittings from only one component of the hyperfine tensor (A_z). In our study, EPR data were collected at multiple microwave frequencies, which allowed us to determine the full A-tensor and extract the

spin-dipolar contributions to the A-tensors. We introduce a new methodology for connecting experimental measurements to density functional theory (DFT)-calculated structures of copper complexes. With this methodology, we identified the metal orbitals containing the unpaired electrons and determined the relative spin density at the metal ion. This analysis established a link between the molecular distortions and the resultant interactions of the unpaired electron in the $d_{x^2-y^2}$ orbital of the Cu^{II} center with the π orbital of $[ibaps]^{3-}$, and this link was experimentally validated through the magnetic hyperfine tensors and the exchange interactions within the complexes.

Results

Preparative Methods of $Bu_4N[Cu^{II}(ibaps)(L)]$ (1-L, where L = OH_2, DBU, TMG, TBD).

The ligand precursor, H_3ibaps, was deprotonated with 3 equiv of KH in tetrahydrofuran (THF) and then treated with $Cu^{II}(OAc)_2$ and water to generate K[**1**-OH_2] and 2 equiv of KOAc, which was removed via filtration (Scheme 1). Without isolation, this potassium salt was metathesized with tetrabutylammonium bromide to afford Bu_4N[**1**-OH_2] in 85 % crystalline yield after recrystallization. To prepare the Cu^{II}–imine complexes, a similar synthetic procedure was followed in which the appropriate imine (DBU, TMG, TBD) was used in place of water – all the Cu-imine complexes were isolated in yields greater than 80 %. We also found that the **1**-imine complexes could be prepared by treating **1**-OH_2 with the appropriate imine ligand in yields that are comparable to those obtained from the more direct route.

Molecular Structures of 1-OH_2 and 1-DBU.

The molecular structure of **1**-OH_2 was determined using X-ray diffraction (XRD) methods to reveal a 4-coordinate Cu^{II} center in a geometry slightly distorted from ideal square planar (τ_4 = 0.22, where τ_4 = 0 for square planar and 1 for tetrahedral, Figure 2, Tables 1 and S1).[37] The nitrogen donor atoms of $[ibaps]^{3-}$ are coordinated in a near-meridional fashion to the Cu^{II} center, with an aqua ligand occupying the final coordination site. The Cu1–N1 bond distance of 1.874(1) Å is significantly shorter than the Cu–N2/3 bond lengths, which average 1.997(1) Å. The Cu–O1 bond length is 1.960(1) Å, which is similar to the distance observed in [Cu(TD1•)(H_2O)] (Cu–O bond length of 1.958 – 1.971 Å).[7] In addition, the phenyl groups within the backbone of $[ibaps]^{3-}$ are slightly skewed, as indicated by an angle of 158° between the planes of the rings.

The structure of **1**-OH_2 also revealed the existence of two intramolecular H-bonds, which form between the aqua ligand and the sulfonamido groups of $[ibaps]^{3-}$, as indicated by the O1…O5 and O3…O5 distances of 2.624(2) and 2.610(2) Å, respectively. The presence of these H-bonds influences the overall structure of **1**-OH_2. For instance, the O atom of the aqua ligand is displaced out of the square plane (N1-Cu1-O5, 166.01(6)°), and an S=O unit on each sulfonamido group is rotated inward to accommodate the formation of the H-bonds. This structural constraint positions the 2,4,6-triisopropylphenyl groups in a syn conformation, and within the crystal lattice, they are nearly coplanar (the angle between the planes of the rings is 172.7°). We note that the molecular structure of a related Ni complex, $[Ni^{II}(ibaps)(OH_2)]^-$, also has analogous intramolecular H-bonds, but the sulfonamido groups

are in an anti-conformation.[36] It thus appears that either conformation can support H-bonds to the aqua ligand.

We also obtained the molecular structure of **1**-DBU and the overall resolution was low because of solvent disorder within the lattice. Although caution should be taken in comparing metrical parameters, the primary coordination sphere around the Cu was well-ordered, allowing the overall coordination geometry and selected metrical parameters to be qualitatively compared to those of **1**-OH_2 (Figures 3A and S1A, Tables S1 and S2). The structure of **1**-DBU revealed a four-coordinate species in which three coordination sites are again occupied by $[ibaps]^{3-}$, and the final site is occupied by the external DBU ligand, which is bound trans to N1 (Figures 3A and S1A). As the DBU ligand lacks any H-bond donors, no intramolecular H-bonds are observed in the molecular structure, allowing for more rotation around the Cu ion than is possible in **1**-OH_2. The bond lengths around the Cu center are similar to those in **1**-OH_2; however, the overall coordination geometry is distorted further away from square planar. For instance, the N1-Cu1-N4 and N2-Cu1-N3 bond angles contract to 159.3(3) and 154.6(2)°, respectively, and the τ_4 value increases to 0.33. Moreover, the appended sulfonamido groups of **1**-DBU are in an anti-conformation, again showing their flexibility around the exogenous ligand.

Electrochemical Properties.

Cyclic voltammetry (CV) was used to evaluate the redox properties of **1**-OH_2 in solution, which are referenced to the $[FeCp_2]^{+/0}$ couple (Figures 4 and S2, Tables 2 and S3). Two reversible one-electron processes were observed in DCM, with $E_{1/2}$ values of −0.48 V (i_a/i_c = 0.81, ΔE = 93 mV) and +0.44 V (i_a/i_c = 1.1, ΔE = 98 mV); similar electrochemical events were found in THF (Table S3). For comparison, [Cu(TD1•)(H_2O)] also has two redox events at $E_{1/2}$ = −0.6 and −0.052 V that are assigned to the (TD1•) ligand.[8] The remaining **1**-TBD, **1**-TMG, and **1**-DBU complexes also exhibited a reversible redox process that is negative of the $[FeCp]^{+/0}$couple (Figures S3–S5, Tables 2 and S3), with each process occurring at potentials more negative than those in **1**-OH_2 (Table S3). A second oxidative event was observed for the **1**-imine complexes but was only **1**-TMG approached reversibility (see SI). We provide spectroscopic evidence that indicates that these redox processes are ligand-localized (see below), which is supported by DFT calculations that reproduce these redox potentials (see SI and Table S4).

Preparation and Properties of the One-Electron (2-L) and Two-Electron (3-L) Oxidized Complexes.

Synthetic routes to the one-electron-oxidized complexes (**2**-L) were successfully pursued for all species using ferrocenium as the oxidant in DCM, and the desired complexes were isolated in yields that ranged from 33 – 87 % (Scheme 2A, SI). The singly oxidized complexes are stable in the solid state and in a 1:1 DCM:THF mixture for >24 hours under an anaerobic environment (Figure S6). We obtained single crystals suitable for analysis by XRD methods for only **2**-TMG; the crystals were grown at −30°C (Figure 3B, Figure S1B). As expected, the Cu center is bound to four N atoms with a single intramolecular H-bond between the NH group of TMG and an O atom in the sulfonamido group of $[ibaps]^{3-}$. In comparison to the molecular structure of **1**-OH_2, the geometry around the Cu center is

more distorted from square planar, with N1-Cu1-N4 and N2-Cu1-N3 angles of 148.5(2)° and 142.8(2)°, respectively. The t_4 value of 0.49 for **2**-TMG is larger than that for **1**-OH_2 and **1**-DBU. These distortions support the premise that the two H-bonds within **1**-OH_2 are enforcing the nearly planar coordination geometry around the Cu center.

The doubly oxidized complexes were generated using two equivalents of tris(*p*-bromophenyl)-ammoniumyl hexafluorophosphate ($MBPF_6$) ($E_{1/2}$ = 0.70 V vs $[FeCp_2]^{+/0}$) in DCM at −80 °C (Scheme 2B). The two systems with reversible redox processes afforded stable complexes, **3**-OH_2 and **3**-TMG; however, **3**-TBD and **3**-DBU were unstable under these conditions, consistent with the irreversibility of their second oxidation event observed by CV and were not further studied.

Infrared Studies.

Solid-state Fourier transform infrared (FTIR) spectra of **1**-L and **2**-L were obtained to investigate the H-bonding interactions of the exogenous ligands (Figure S7). The **1**-OH_2 complex showed a broad, weak ν(OH) at 3180 cm^{-1} that shifted to 2424 cm^{-1} upon deuteration (ν(OH)/ν(OD) = 1.31; calcd. 1.37, Table 3, Figure S7). The *ν*(OH) feature for **2**-OH_2 was observed at a slightly higher energy of 3225 cm^{-1} and was also isotopically sensitive. FTIR spectra of the imine compounds excluding **1**-DBU also revealed broad, weak features, which are attributed to the NH moieties; these features appear at 3300 cm^{-1} and 3335 cm^{-1} for **1**-TBD and **1**-TMG, respectively. Oxidation of the imine complexes also shifted the ν(NH) bands to slightly higher energies (Table 3). The broadness and relatively low energies of the *ν*(OH) and ν(NH) features are attributed to the presence of intramolecular H-bonds to the exogenous ligand that were observed in the molecular structures of **1**-OH_2 and **2**-TMG and that are presumed to be present in the other complexes.[38–40] Moreover, the changes observed in these frequencies upon oxidation could be caused by a weakening of the H-bonds. The FTIR spectra of **1**-DBU and **2**-DBU do not contain any features higher in energy than 3050 cm^{-1}, consistent with the absence of NH bonds in these systems.

Electronic Absorption Properties.

The electronic absorption spectra of the **1**-L complexes in 1:1 DCM:THF at room temperature exhibited relatively weak features centered around 340 nm, ~530 nm, and 1000 nm (Figure 5A, Table 3). Time-dependent (TD)-DFT analysis (see below) assigned these bands to primarily ligand π to Cu^{II} $d_{x^2-y^2}$ charge transfer transitions. The absorption spectra for the **2**-L complexes contain several new, more intense bands, notably a low-energy feature with λ_{max} values that range from 865 to 965 nm and molar extension coefficients between 2700 and 8400 $M^{-1}cm^{-1}$ (Figure 5B, Table 3, Figures S8–S11). Complexes **2**-TBD, **2**-TMG, and **2**-DBU could also be generated through the addition of the imine reagent to **2**-OH_2 (Figures S12–14). Note that the one-electron oxidation processes to generate **2**-L are reversible: reversion to the spectra of the **1**-L complexes was accomplished using cobaltocene (Figures S15–S18). Bands with similar λ_{max} values and extinction coefficients as those of the **2**-L complexes have been reported for other complexes with $[NNN]^{3-}$ redox-active ligands and have been assigned to ligand-centered transitions. For instance, comparable features have been observed in complexes from the Heyduk group with

λ_{max} = 1035 nm (4500 $M^{-1}cm^{-1}$),[21] the [Cu(TD1•)(H_2O)] complex from the Tomat group with λ_{max} = 932 nm,[8] and ^{tBu}CuOH from the Garcia-Bosch group at λ_{max} = 950 nm (4000 $M^{-1}cm^{-1}$).[9] Moreover, we have previously characterized the one-electron-oxidized complex [Fe(ibaps)(bpy)], which also exhibited an NIR feature at λ_{max} = 1025 nm (4080 $M^{-1}cm^{-1}$) that was attributed to a ligand-centered radical.[35] Finally, the spectral features of the two-electron-oxidized species **3**-OH_2 and **3**-TMG (Figure 5C, Table 3) are similar to those of the $[Cu^{II}(^{R}L)]^{+}$ complexes from Storr and Thomas, where R = H or Ph (Figure 1D).[10,41] Both of these $[Cu^{II}(^{R}L)]^{+}$ species from Storr and Thomas were determined to have ligands that were oxidized by two electrons, and their electronic absorption characteristics were assigned to ligand-based transitions.

Magnetic Properties.

X- and S-band EPR spectra (Figures 6, 7) of the **1**-L complexes showed signals indicative of $S = {}^{1}/_{2}$ spin ground states. From the spectra collected at two microwave frequencies, the full g and hyperfine A-tensors of the complexes could be determined (Table 3). As expected, the lower microwave frequency (S-band) enhanced the resolution of the $^{63/65}$Cu and ^{14}N hyperfine splittings. For each complex, the second derivative of the S-band spectrum further enhanced the resolution of the ^{14}N hyperfine splitting (Figure 7, green spectra). Simulations were generated for the spectra via simultaneous least-squares fitting of the X-band, S-band, and S-band 2nd derivative spectra and are overlaid on the data (thin black lines). The spectral fits included second-order perturbation of the Cu hyperfine term in the spin Hamiltonian because of the large $^{63/65}$Cu hyperfine constants. The simulations were sensitive to the number of ^{14}N nuclei within each complex, allowing us to determine the total number of N atom donors coordinated to the Cu center in each complex. For **1**-OH_2, the best fits occurred when three ^{14}N nuclei were included and two of them were assumed to be equivalent. DFT calculations supported this assumption, as the N atoms of the sulfonamido groups had approximately equal spin densities, which were smaller than that found on the central amine nitrogen. For the **1**-imine complexes, the simulations required four ^{14}N nuclei, which was the initial indication that the added imines had substituted for the water ligand rather than deprotonating it. DFT calculations found that the coordinated N atoms of the imine ligands (TBD, TMG, and DBU) gave a significantly lower spin density than the N atoms of $[ibaps]^{3-}$. Based on this finding, the **1**-imine simulations assumed that three of the four coordinated N atoms were equivalent. The isotropic values of their ^{14}N A-tensors (Table 3) are typical of Cu complexes with nitrogen-donating ligands.[42]

In general, we obtained excellent fits of the ^{14}N hyperfine structure, which were important in our determination of accurate values for the x and y components of the Cu A-tensor (Table 3). For the **1**-imine complexes, the A_z values and isotropic value of the A-tensor (A^{iso}) for the Cu centers were significantly lower than those of **1**-OH_2. We attribute this difference to the donation of more electron density from the $[ibaps]^{3-}$ ligand into the Cu^{II} $d_{x^2-y^2}$ orbital (see Discussion). While the magnitude of the A-tensor components can be determined from the spectra, their signs cannot be obtained directly. However, Cu^{II} A^{iso} values are negative,[43] and we used this fact in our analyses. The values of A_x and A_y for **1**-TMG are near zero, and therefore, the value of A_z must be negative, and A^{iso} = −160 MHz. The values of A_y for

1-TBD and **1**-DBU required a positive sign (Table 3) to give values of A^{iso} close to that of **1**-TMG.

Magnetic Properties of 2-L.

Upon oxidation of the **1**-L complexes, the EPR spectra associated with the Cu^{II} species vanished. Only **2**-OH_2 produced a new EPR signal that was observed in parallel mode at g = 4.1 with a 4-line hyperfine splitting of 6.5 mT (Figure 8). The signal position is indicative of a transition between the $|1^+>$ and $|1^->$ levels of an $S = 1$ spin system, where $|1^\pm> = |1> \pm |-1>$ are the zero-field spin states. The $S = 1$ state is produced from ferromagnetic exchange coupling between the $S = \frac{1}{2}$ Cu^{II} site and an $S = \frac{1}{2}$ ligand radical ($[ibaps\cdot]^{2-}$) with the 4-line hyperfine pattern arising from the $^{63/65}Cu$ nucleus, which has a nuclear spin (I) of 3/2. The temperature dependence of the signal (see inset) was analyzed with an $S = 1$ spin Hamiltonian to give a zero-field splitting constant (D) of +3.4(4) cm^{-1}. The positive sign of D is indicative of a spin system in which the $m_s = 0$ level is the ground state and the $|1^\pm>$ levels are excited states within the $S = 1$ manifold. The simulation overlaid on the spectrum (Figure 8) is for $S = 1$ with $g_z = 2.06$ and $A_z = 195$ MHz and is quantitative for the sample concentration. The conversion from the system spin $S = 1$ to the local $S = \frac{1}{2}$ Cu^{II} site gives $g_z^{Cu} = 2.12$ and $A_z^{Cu} = 390$ MHz ($A_{S=1/2} = 2A_{S=1}$).[51] The large Cu hyperfine coupling is consistent with the oxidation of the $[ibaps]^{3-}$ ligand. The large zero-field splitting is due to spin-orbit coupling with an excited orbital configuration (see below). The significant change in the g_z and A_z values of **2**-H_2O from those in **1**-H_2O is caused by a rotation of the D-tensor relative to the axis of the doubly occupied d_{z^2} orbital owing to mixing of the d_{xz} and d_{xy} orbitals arising from the distortion of the ligand plane. For a rotation of 45° relative to the Cu^{II} electronic coordinate system, the g and A values observed for the local $S = \frac{1}{2}$ Cu^{II} site of **2**-H_2O are reduced from 2.20 and 570 MHz in **1**-OH_2 to 2.12 and 390 MHz. The addition of cobaltocene to the **2**-L complexes regenerated the EPR spectra of the respective **1**-L complexes (Figures S19–S22).

The **2**-imine complexes were investigated using NMR spectroscopy, which revealed diamagnetic spectra for all three species (Figures S23–S26). These results are consistent with the lack of observable EPR signals and suggest that $S = 0$ spin ground states are achieved through antiferromagnetic coupling between the Cu^{II} center and $[ibaps\cdot]^{2-}$. Using a combination of ^1H, gCOSY, and gNOESY spectroscopies and the addition of D_2O, the proton assignments were made for each complex (Figures S27–S32). To corroborate the electronic assignments established by UV-vis, EPR, and NMR experiments, X-ray absorption near-edge spectral (XANES) data were collected for a subset of **1**-L and **2**-L complexes (see SI). For all the complexes analyzed (**1**-OH_2, **1**-TBD, **2**-OH_2, and **2**-TBD), the pre-edge features were centered at ~8979 eV (Figure S33, Table S5). This value falls in the range for Cu^{II} ions and is consistent with the valence at the Cu centers being unchanged by oxidation.[44,45]

Magnetic Properties of 3-L.

The two-electron-oxidized complexes, **3**-OH_2 and **3**-TMG, gave Cu^{II} X- and S-band EPR spectra that were different from those of their precursors (Figures S34 and S35). Both complexes showed spectra with large hyperfine constants (Table 3), indicating that the second oxidation event also occurs in the [NNN] ligand, generating $[ibaps]^{\cdot-}$.

Computational Analyses.

DFT calculations were performed to obtain the optimized structures of the **1**-L complexes. The DFT-calculated structure of **1**-OH_2 agrees with that obtained by XRD methods and has a distorted square planar coordination geometry. The N1–Cu–O1 and N2–Cu–N3 bond angles are greater than 160°, and the two aryl groups of $[ibaps]^{3-}$ are slightly skewed in the same manner as observed experimentally (see above). The unpaired electron occupies the Cu $d_{x^2-y^2}$ orbital, which is antibonding to the sp^2/sp^3 orbitals of the $[ibaps]^{3-}$/aqua ligands (Figures 9, S36–S37). The ligand orbitals transfer β-electron density into the half-filled Cu $d_{x^2-y^2}$ orbital, resulting in spin polarization on the N atoms, which contributes to the observed ^{14}N hyperfine splitting in the EPR spectra. The largest spin polarization appears on the central N donor (N1).

Similar to the XRD structure of **1**-DBU, DFT calculations found that the structures of the **1**-imine complexes are more distorted from square planar than that of **1**-OH_2 (Table 4). The smaller N2-Cu-N3 angle is principally caused by a shift of the Cu atom away from N1 within the plane defined by the three N atoms of the $[ibaps]^{3-}$ ligand. The changes in the molecular structures from **1**-OH_2 to the **1**-imine complexes depend on the steric and H-bonding interactions between the ancillary ligand and $[ibaps]^{3-}$ and the electronic interactions affecting the bonds between the Cu center and the $[ibaps]^{3-}$ ligand. We will show that the H-bonds within **1**-OH_2 are the main cause of the structural differences, but first, we will explore the specifics of the electronic structure of $[ibaps]^{3-}$ that led to a distortion away from a square planar coordination geometry. The HOMO in all the **1**-L complexes is a p orbital principally centered on $[ibaps]^{3-}$, and the largest amplitude is at the N1 p_z orbital (Figure 9, bottom). For **1**-OH_2, s-bonding dominates, and the N1 p_z orbital is barely involved in bonding because the Cu $d_{x^2-y^2}$ orbital is nearly aligned with the nodal plane of the redox-active p orbital of $[ibaps]^{3-}$. The spin density on N1 thus more closely aligns with the Cu–N1 vector to form a predominately s-bond between the N1 sp^2 and Cu $d_{x^2-y^2}$ orbitals (Figure 10, top). For the **1**-imine complexes, the Cu $d_{x^2-y^2}$ orbital is tilted away from the nodal plane, which creates a non-orthogonal orbital arrangement (an overlap analysis is given in the SI), resulting in bond formation between the tilted Cu $d_{x^2-y^2}$ orbital and the N1 p_z orbital (Figure 10, bottom). The additional d-p_z bonding interaction derived from this distortion results in the transfer of β-electron density from the p_z orbital into the half-filled Cu $d_{x^2-y^2}$ orbital. For **1**-TBD (Figure 10, bottom-right), the β density transfer from both the sp^2 and p_z orbitals causes the net spin density on N1 to be rotated away from the Cu-N1 vector. The additional spin transfer reduces the spin population of the Cu $d_{x^2-y^2}$ orbital, which lowers the magnitude of the experimental A values for the Cu^{II} center (Table 4). These findings indicate that the rotation of the spin density at N1 is not due to a structural

change within $[ibaps]^{3-}$ (e.g., change in the orientation of the C-N1-C angle) but rather the resultant combination of spin densities from both sp^2 and p_z orbitals.

We also considered whether the observed structural and electronic properties of the Cu complexes could be sterically induced rather than rooted in the redox-active nature of $[ibaps]^{3-}$. To distinguish between these two possibilities, we performed DFT calculations for a truncated model in which the sulfonamido O atoms and aryl groups have been replaced by hydrogen atoms (denoted $[ibaps^{\mathbf{T}}]^{3-}$, Figures S38–S40). These calculations were performed over the three experimentally investigated oxidation levels with water, ammonia, imine $H_2C{=}NH$, and the TBD and DBU molecules as ligands ($[Cu(ibaps^{\mathbf{T}})L]^n$, Table 5). For the Cu complexes of both $[ibaps]^{3-}$ and $[ibaps^{\mathbf{T}}]^{3-}$, the one- and two-electron oxidations remove electrons from the ligand p HOMO with the largest amplitude at the central N atom of the tridentate ligands. A key outcome of the computational studies is the similarity in the properties, including coordination geometries, of the $[Cu(ibaps^{\mathbf{T}})L]^n$ complexes to those found for $[Cu(ibaps)L]^n$, with the exception of L = H_2O. (Figures S38–S40, Tables 5). For instance, the computed structures of both the truncated $\mathbf{1}^{\mathbf{T}}$-imine and **1**-imine complexes gave similar N2–Cu–N3 angles and L-Cu-N1 angles of less than 160°. These calculations indicate that intrinsic electronic factors play a role in the control of the L-Cu-N1 angle. Compared to the $\mathbf{1}^{\mathrm{T}}$-OH_2 complex, which has a small H_2O-Cu-N1 angle (131°) like those found in the $\mathbf{1}^{\mathrm{T}}$-imine complexes, the optimized **1**-OH_2 complex has a markedly larger angle (166°, Table 5). We attribute the large L-Cu-N1 angle in **1**-OH_2 to geometric constraints imposed by the intramolecular H-bonds of the aqua ligand to the O atoms of the sulfonamido groups. We note that in the DFT calculations of $\mathbf{1}^{\mathrm{T}}$-OH_2, one of the lone pairs of the aqua ligand was constrained to be directed toward the Cu center throughout the optimization (see SI). Without this constraint, the Cu–O bond breaks, and the water molecule reorients to form an H-bond with N2 or N3, thus indicating that the water is weakly coordinated to Cu.

Our computational studies considered two possibilities for the one-electron-oxidized species (Tables 5 and S9): 1) the antiparallel spin configuration (broken symmetry) in which the **2**-imine complexes retained the L-Cu-N1 angles of < 160°, and 2) the parallel spin state (ferromagnetic coupling) where the angle is consistently near 180° for the truncated species. The relative energies and bond angles of these two calculated states were compared, and our analysis found that the smaller angles in the antiparallel spin configuration are a consequence of the nascent tilted $d_{x^2-y^2} - p_z$ bonding interaction, as discussed above for **1**-L and $\mathbf{1}^{\mathrm{T}}$-L. This tilted $d_{x^2-y^2} - p_z$ bond is prevented by the Pauli principle in the parallel spin state, resulting in nearly linear L-Cu-N1 angles. Again, the broken symmetry state of **2**-OH_2 is the exception owing to the two intramolecular H-bonds, and thus, the parallel spin configuration is favorable with a lower energy than the broken symmetry configuration (ΔE < 0 in Table 5), as observed using EPR spectroscopy.

For the two-electron-oxidized complexes (**3**-L), DFT results gave different L-Cu-N1 angles for the Cu complexes with $[ibaps]^{1-}$ versus $[ibaps^{\mathbf{T}}]^{1-}$ ligands (Table 5). For the $\mathbf{3}^{\mathrm{T}}$-L complexes, the now-empty π orbital cannot donate into the Cu $d_{x^2-y^2}$ orbital, resulting in L-Cu-N1 angles of nearly 180°. The same angle computed for the **3**-L complexes deviates

from linearity with angles between 149° and 172°; thus, the calculations of these complexes indicate that the imine ligands have either steric or H-bond interactions that also contribute to the smaller L-Cu-N1 angles.

Electronic Absorption Properties.

Computed electronic absorption spectra obtained from TD-DFT calculations for the **1**-OH_2 and **1**-TMG complexes (see SI, Figures S41–S42) revealed that the absorption bands between 500 and 1000 nm are ligand-to-metal charge transfer (LMCT) transitions ($\pi \rightarrow$ Cu $d_{x^2-y^2}$) involving the π orbitals of $[ibaps]^{3-}$. The lowest-energy band at $\lambda_{max} \sim 1000$ nm is predominately the LMCT transition π HOMO → Cu d_{x^2-y2}. The overall greater absorption of **1**-TMG relative to **1**-OH_2 is ascribed to a higher degree of non-planarity in the Cu coordination of the Cu-imine complex. The **2**-L and **3**-L complexes, in which electrons are removed from the redox-active π orbital, introduces additional intra-ligand charge transfer transitions in the visible range – these transitions involve the transfer of an electron into the vacated π orbital on $[ibaps]^{2-/1-}$ (Figure S43).

We used DFT computations to also account for aspects of our EPR results. In particular, the experimentally determined isotropic and A_z values of **1**-OH_2 are significantly larger in magnitude than those of the **1**-imine complexes (Table 3). To understand this trend, we performed a comparative analysis of the A_z^{SD} values (SD, spin-dipole) evaluated by DFT. The A-tensor has three contributions: $\mathbf{A} = A^{iso} + \mathbf{A^{SD}} + \mathbf{A^{SO}}$, from isotropic contact, spin-dipolar, and spin-orbit coupling, respectively, and thus, $A_z^{SD} = A_z - A^{iso} - A_z^{SO}$. The values of A_z and A^{iso} are experimentally determined (Table 3), and the spin-orbit contribution was obtained from eq 1

$$A_Z^{SO} = P\left\{-\frac{5}{42}(\Delta g_x + \Delta g_y) + \frac{2}{3}\Delta g_z\right\} \quad (1)$$

where $\Delta g_i = g_i - 2 (i = x, y, z)$ (Tables 3 and S6).[46] The value of P, which is a function of the radial distribution of d electrons in a free metal ion, has been treated as an adjustable parameter for incorporating the influence of the covalency of the Cu-ligand bonds on the magnetic hyperfine interactions. For **1**-L and **3**-L, the values of P that gave the best agreement with the DFT results were 1000 MHz and 1300 MHz, respectively, which are in the expected range for Cu^{II} complexes.[46] As stated above, the signs of the A values are not determined from experiment, but Cu^{II} A^{iso} values are known to be negative. We considered all possible sign combinations of the components of the A-tensor (see SI, Tables S7 & S8) to obtain the experimental A_z^{SD} values for each complex (Table 6), which agreed with those found by DFT calculations (Table 6). The large negative A_z^{SD} value reflects the predominant Cu $d_{x^2-y^2}$ character of the unpaired electron. Complex **1**-OH_2 has an L-Cu-N1 bond angle > 160° and a large coupling of $\left|A_z^{SD}\right| > 450$ MHz. In contrast, the analogous **1**-imine complexes have L-Cu-N bond angles < 160° and have smaller couplings, with values of $\left|A_z^{SD}\right|$ significantly below 450 MHz.

Discussion

Cu Complexes that Span Three Oxidation Levels.

The Cu complex of $[ibaps]^{3-}$ can readily coordinate an external ligand to produce a series of four-coordinate, mononuclear Cu complexes ($[Cu^{II}(ibaps)L]^{-}$) in which the fourth ligand (L) is either water or an imine (DBU, TBD, or TMG). We also found that the **1**-imine complexes could be prepared directly from **1**-OH_2 via ligand substitution – we recognize that imines are often used as Brønsted bases, but in the case of **1**-OH_2, substitution chemistry is more favorable than deprotonation of the aqua ligand. The relatively short Cu-N1 bond (1.874(1) Å) found in the structure of **1**-OH_2 would lead to a considerable trans effect that resulted in the facile displacement of the aqua ligand. Moreover, our computational studies suggested that the Cu–O1 interaction is weak, and the isolation of **1**-OH_2 was aided by intramolecular H-bonds involving the aqua ligand.

All the **1**-L complexes possess two redox processes, most of which were accessed using chemical oxidants to afford one-electron (**2**-L) and two-electron-oxidized (**3**-L) species. Our spectroscopic and computational studies agree that both oxidations are centered on the $[ibaps]^{3-}$ ligand, with the Cu center remaining in the 2+ valence state. For instance, the absorption spectra of the **2**-L and **3**-L complexes resemble those reported for the oxidized forms of complexes with [NNN] redox-active ligands.[9,10,21,35,36,41] The isolation of **1**-L, **2**-L, and **3**-L provided an opportunity to examine the effects of the ancillary ligands on both the molecular and electronic structures and the impact of intramolecular H-bonds in regulating magnetic coupling between a metal center and a multidentate, redox-active ligand.

Interplay Between the Cu Center and $[ibaps]^{3-}$.

Distortion away from square planarity in four-coordinate Cu^{II} complexes is often achieved through secondary coordination sphere effects, such as steric constraints imposed by ligands. Our studies on $[Cu^{II}(ibaps)L]^{-}$ discovered another contributor to molecular non-planarity which involves the redox-active electron(s) of $[ibaps]^{3-}$ that occupy a π orbital. *The interplay of this ligand π orbital with the Cu* $d_{x^2-y^2}$ *orbital has a profound effect on the structure and electronic properties of the complexes.* We computationally explored these effects for the **1**-L complexes. For planar structures, the Cu $d_{x^2-y^2}$ orbital is centered at the nodal plane of the π orbital of $[ibaps]^{3-}$, leaving the two orbitals orthogonal because they have different symmetries under reflection with the xy-plane. For non-planar structures, the mirror symmetry is broken, and a d-p_z bond occurs between the tilted Cu $d_{x^2-y^2}$ orbital and the π orbital of $[ibaps]^{3-}$ (Figure 10, bottom). Cu^{II} complexes are generally square planar because of strong σ bonding. The energies of the ligand π orbitals are generally significantly lower than that of the Cu orbital containing the unpaired electron, which precludes additional bonding interactions. This is not the case for the **1**-L complexes because the redox-active orbital on $[ibaps]^{3-}$, of which the largest amplitude is at the central nitrogen atom, N1, is close in energy to the Cu $d_{x^2-y^2}$ orbital. As the angle L-Cu-N1 deviates appreciably from 180°, the strength of the d-p_z bond increases and stabilizes a non-planar Cu coordination geometry. However, the angular bending also weakens the s bonds, and

thus, the stability of the complexes depends on the L-Cu-N1 angle that best balances the σ and d-p_z bonding interactions to give the lowest overall energy. The outlier in this series is **1**-OH_2, which has a relatively large L-Cu-N1 angle of 166° that is caused by the structural constraints imposed by the presence of two intramolecular H-bonds. Removal of these interactions in the truncated complex ($[Cu(ibaps^{\mathbf{T}})OH_2]^{n-}$ resulted in a substantially smaller angle of 131° (Table 6). The presence of a H-bond in **1**-TMG, illustrated in **2**-TMG (Figure 3), prompted us to examine why this interaction does not lead to a more linear N1-Cu-L angle like in **1**-OH_2. Our studies on **1**-OH_2 (Figure 2) show that it has two intramolecular H-bonds which appear to be stronger (DFT: H · O 1.71 Å) than the single H-bond in **1**-TMG (DFT: H · O 2.07 Å). In addition, **1**-TMG has, among the three **1**-imine complexes, the largest N1-Cu-L angle which may influence the H-bond. The H · O H-bond in **1**-TMG would have been stronger with a more linear N1-Cu-L angle, but the d-p_2 bonding interaction (Figure 10) prevents this from occurring; thus, the observed angle is a compromise between these two competing bonding interactions. For **1**-TBD, the N1-Cu-L angle is smallest among the Cu-imine complexes and may be influenced by a weak H-bond between the NH group of the TBD ligand and the lone pair at N1 (DFT: H · N1 2.59 Å) that could contribute to the shortening the N1-Cu-L angle. There are no intramolecular H-bonds in **1**-DBU and the N1-Cu-L angle is between those in **1**-TMG and **1**-TBD because it is solely regulated by the orbital mechanism outlined above.

Evidence for the importance of the L-Cu-N1 angle in the determination of the electronic properties comes from correlations between the computed structural parameters and the experimentally determined spectroscopic data. In particular, the interplay between the redox-active ligand π orbital and the tilted Cu $d_{x^2-y^2}$ orbital affects the observed hyperfine constants of the Cu centers. For L-Cu-N1 angles with large deviations from 180° (that is, for the **1**-imine complexes), the additional d-p_z bonding interaction increases the transfer of electron density from the ligand p orbital into the Cu $d_{x^2-y^2}$ orbital. This transfer thus results in a reduction of the spin population at the Cu center, which lowers the magnitude of the Cu A_{iso} and A_z^{SD} values (spin densities are listed in SI). In addition, the DFT-calculated A_z^{SD} values agree with those values determined experimentally, supporting the correlation between the experimental L-Cu-N1 angle and the observed A values (Tables 3 and 6). For **1**-OH_2, the magnitudes of the A values are larger because the two intramolecular H-bonds enforce an O5-Cu-N1 angle closer to linear. Furthermore, our analysis also applies to the Cu^{II}–hydroxide complex of Garcia-Bosch (^{tBu}CuOH, Figure 1) that has a similar design as **1**-OH_2 with two intramolecular H-bonds between urea groups and a hydroxide ligand. The molecular structure of ^{tBu}CuOH obtained from DFT calculations showed a nearly square planar coordination geometry, including an O-Cu-N1 angle of 160° with an observed A_z value (540 MHz) close to that of **1**-OH_2 (570 MHz).

The important role of d-p_z bonding found for the **1**-L complexes is absent in nearly all other Cu complexes reported in the literature. For instance, the Cu-aqua complex with the tridentate ligand N,N'-bis(2,6-diisopropylphenyl)-2,6-pyridinedicarboxamide (**4**-OH_2, Figure S44) has an O-Cu-N_{py} angle of ~180° despite the lack of any enforcing H-bonds as in **1**-OH_2.[47] The tridentate ligand in **4**-OH_2 utilizes a central pyridine that interacts differently with the Cu $d_{x^2-y^2}$ orbital because the occupied π orbitals of the pyridine are delocalized

and significantly lower in energy relative to the redox-active π orbital in $[ibaps]^{3-}$. This difference can be observed in the energies of the LMCT bands for the two complexes. The absorption spectrum of **1**-OH_2 shows a band with $\lambda_{max} \sim 1000$ nm that is predominately a N1 p_z to Cu $d_{x^2-y^2}$ charge transfer transition. In contrast, the lowest pyridine to Cu $d_{x^2-y^2}$ charge transfer transition in **4**-OH_2 has a peak with $\lambda_{max} \sim 300$ nm (see SI for details, Figure S45), indicating that the energy gap between the p orbitals and the Cu^{II} $d_{x^2-y^2}$ orbital in this complex is much larger than that in **1**-OH_2. Consequently, distortions of the complex that would allow N_{py} π/Cu $d_{x^2-y^2}$ overlap do not effectively compete with the σ bonds that prefer an O-Cu-N_{py} angle of ~180°. To provide further evidence for the role of the [NNN] ligands in the bending mechanism, we have also investigated the L-Cu-N_{py} angle when the water ligand in **4**-OH_2 is replaced by the TBD ligand. DFT optimization showed that the structure of this hypothetical complex has a linear L-Cu-N_{py} unit and a large A_z^{SD} value typical for square planar Cu^{II} complexes, unlike the DFT structure of **1**-TBD in which the L-Cu-N1 unit is bent and A_z^{SD} is small. As the two species have the same ancillary TBD ligand, any difference between them must be rooted in the properties of the [NNN] ligands supporting these systems.

Oxidized Complexes.

Further evidence for the interplay between the redox-active ligand π orbital and Cu $d_{x^2-y^2}$ orbital is observed from the oxidized complexes. The **2**-L complexes have an unpaired electron in the SOMO π orbital of $[ibaps\cdot]^{2-}$ that couples with the unpaired electron in the Cu $d_{x^2-y^2}$ orbital to afford either an $S = 0$ or $S = 1$ state. For **2**-OH_2, the near-linear O1-Cu-N1 angle enforced by the intramolecular H-bonds causes the Cu $d_{x^2-y^2}$ and p orbitals to be nearly orthogonal. According to the Kanamori-Goodenough rules,[48–50] orthogonal magnetic orbitals give ferromagnetic coupling of electron spins ($S = 1$, ground state). Indeed, the predicted $S = 1$ ground state for **2**-OH_2 is observed with parallel-mode EPR methods.

Complex **2**-OH_2 has a large zero-field splitting ($D_{exp} = 3.4\ cm^{-1}$) that is a consequence of anisotropic exchange owing to spin-orbit coupling at the Cu center. Experimental evidence for such large values of D for Cu^{II}-radical complexes is rare; for example, D values from Cu^{II}-nitroxide complexes are less than 0.2 cm^{-1}.[51] The **2**-OH_2 complex has a set of *d*-*d* transitions similar to those in **1**-OH_2, with $\Delta_{yz \rightarrow x^2-y^2} = 2.87$ eV, $\Delta_{xy \rightarrow x^2-y^2} = 2.73$ eV, and $\Delta_{xz \rightarrow x^2-y^2} = 2.29$ eV. To understand the magnitude and sign of this D, we derived eq 2 (see SI) for determining D values in terms of the g value for the coupled $S = 1$ spin state (g = 2.06) and the exchange coupling (J_{xz}) for the excited $d_{xz} \rightarrow d_{x^2-y^2}$ electronic configuration, which is admixed into the ground state by spin-orbit coupling, thereby yielding unquenched orbital momentum along y.

$$D = D_y = \frac{5}{32}(g_y - 2)^2 J_{xz} \quad (2)$$

The d_{xz} orbital has non-orthogonal overlap with the central p_z orbital, which contains most of the unpaired electron in $[ibaps\cdot]^{2-}$, thus giving a strong antiferromagnetic interaction ($J_{xz} > 0$). Meanwhile, the d_{xy}, d_{yy}, and d_{z^2} orbitals, which are perpendicular to the p_z orbital, give weak ferromagnetic couplings. Equation 2 predicts $D > 0$ in agreement with the experimental data and using the experimental value for D gives $J_{xz} = 6000\ cm^{-1}$. The exchange coupling is expected to have a magnitude typical of a coordination bond (~1 eV) given the large overlap between the Cu d_{xz} and redox-active p_z orbitals.

The $S = 0$ state, which has the two-electron spin function $\alpha\beta - \beta\alpha$, cannot be rigorously treated by DFT, and instead, we use the broken symmetry state with spin function $\alpha\beta$. Like the true $S = 0$ state, the broken symmetry state allows N1 p_z – Cu $d_{x^2-y^2}$ charge transfer and nascent d-p_z bond formation, resulting in the small L-Cu-N1 angles (Table 5). In contrast, the N1 p_z – Cu $d_{x^2-y^2}$ charge transfer interaction is forbidden by the Pauli principle in the ferromagnetic state ($S = 1$). Thus, the L-Cu-N1 angle is strongly correlated with the magneto-chemical properties of the complexes. A nearly linear angle leads to the orthogonality of the magnetic orbitals and results in a paramagnetic complex, whereas smaller angles cause a switch to antiferromagnetic coupling to give diamagnetic complexes. The DFT-calculated energy differences between the two spin states ($\Delta E = E_{ferro} - E_{broken\ symm}$, Table 5) show that only **2**-OH_2 is ferromagnetic ($\Delta E < 0$). The literature reports several four-coordinate Cu-ligand radical complexes that exhibit ferromagnetic exchange coupling ($S = 1$).[7,8,13,52] The metal-ligand bonds in these complexes are dominated by σ interactions that produce planar coordination geometries and orthogonal magnetic orbitals (Figure 10, top left)

The two-electron oxidation of **1**-L removes two electrons from the HOMO π orbital of $[ibaps]^{3-}$, leaving this orbital unoccupied in the **3**-L complexes. The d-p_z bonding described in Figure 10 is then absent, and the complex cannot lower its energy by decreasing the L-Cu-N1 angle. Thus, the DFT calculations for the truncated $\mathbf{3}^{T}$-L complexes gave L-Cu-N1 angles that are nearly linear. However, our DFT calculations for the **3**-imine complexes gave nonlinear L-Cu-N1 angles (Table S11). Furthermore, the experimental A_{iso} and A_z values for the Cu center in **3**-TMG were lower than the values for **3**-OH_2, and the A_z^{SD} values agree with the DFT-calculated values (Tables 3 and 6). The L-Cu-N1 angle in the **3**-L complexes may have become more susceptible to steric influences than in the **1**-L complexes, as the two-electron oxidation of the ligand has lessened the σ donations that stabilize the square planar coordination geometry. The lower σ electron donation and the accompanying increase in the spin population of the Cu^{II} site is in keeping with the increase in the P value for the two-electron-oxidized complexes that was noted above.

Summary and Conclusions

Copper(II) complexes have long been known to form mononuclear, square planar complexes in which σ bonding dominates because the π orbitals of the ligands are usually at a significantly lower energy than the Cu d orbitals. The present studies have shown that this bonding scenario is not the case in Cu complexes with the [NNN] redox-active ligand $[ibaps]^{3-}$: the significant degree of localization of the redox-active π orbital at the central

nitrogen atom of the $[ibaps]^{3-}$ ligand brings the π orbital energetically and spatially close to the half-filled Cu d orbital. The similarity of these orbital energies allows **π** interactions to compete with σ bonding in the $[Cu(ibaps)L)]^{n}$ complexes, causing deviations from planarity. These deviations enable the redox-active ligand π orbital in **1**-L and **2**-L to interact with the half-occupied Cu $d_{x^2-y^2}$ orbital, thereby lowering the energy of the system. In the absence of steric or H-bonding interactions of the ancillary ligand with $[ibaps]^{3-}$, we have pinpointed that changes in the L-Cu-N1 angle are caused by a nascent d-p_z bond, producing the observed non-planar coordination geometries. The effects of this additional bonding interaction are experimentally evident from changes in both the copper-ligand radical exchange interactions and the copper hyperfine values. The $S = 1$ state of **2**-OH_2 is attributed to the aqua ligand forming intramolecular H-bonds with the $[ibaps\cdot]^{2-}$ ligand that enforce an O-Cu-N1 angle of greater than 160°. In contrast, the **2**-imine complexes are all diamagnetic at room temperature because distortions in the equatorial plane around the Cu center (e.g., N_{imine}-Cu-N1 angles of less than 160°) lead to strong antiferromagnetic coupling between the spins at the Cu^{II} center and $[ibaps\cdot]^{2-}$. The smaller N_{imine}-Cu-N1 angles in the **2**-imine complexes are also shown to closely correlate with the copper hyperfine values. The discovery of this correlation required the introduction of a new methodology to establish a quantitative connection between the experimental hyperfine measurements and DFT structural calculations for copper complexes.

Prior to this investigation there were no reports of metal-[NNN] complexes that support both ferromagnetic and antiferromagnetic couplings depending on the choice of the exogenous ligand. In heme enzymes, it is suspected that the coordination of exogenous ligands controls the exchange coupling between Fe and ligand-based spins (see above),[34] although the mechanism for regulating the exchange-coupling constant has yet to be established. Our proposed exchange mechanism is sensitive to modulations of a single metal-ligand bond angle (by <20 ° between resulting spin states changes) which for the [Cu(ibaps)L] complexes, is influenced by intramolecular H-bonds to cause different magnetic characteristics. Therefore, the balance between a nascent d-p_z bond and H-bonds illustrates a new type of control over the structure and properties of metal complexes and adds a conceptual tool in the design of molecular devices and reactive reagents.

Supplementary Material

Refer to Web version on PubMed Central for supplementary material.

ACKNOWLEDGMENT

The authors acknowledge the NIH (GM050781 to A.S.B. and GM077387 to M.P.H.) for funding and the UCI Department of Chemistry for fellowships to D.L.R.

References

1. McEvoy JP; Brudvig GW Water-splitting chemistry of photosystem II. Chem Rev 2006, 106, 4455–4483. [PubMed: 17091926]
2. Einsle O; Rees DC Structural Enzymology of Nitrogenase Enzymes. Chem Rev 2020, 120, 4969–5004. [PubMed: 32538623]

3. Labinger JA; Bercaw Arnold JE; Beckman M Understanding and exploiting C-H bond activation. Nature 2002, 417, 507–514. [PubMed: 12037558]
4. Chirik PJ; Wieghardt K Radical Ligands Confer Nobility on Base-Metal Catalysts. Science (1979) 2010, 327, 794–795.
5. Pegis ML; Wise CF; Martin DJ; Mayer JM Oxygen Reduction by Homogeneous Molecular Catalysts and Electrocatalysts. Chem Rev 2018, 118, 2340–2391. [PubMed: 29406708]
6. Nguyen AI; Blackmore KJ; Carter SM; Zarkesh RA; Heyduk AF One- and Two-Electron Reactivity of a Tantalum(V) Complex with a Redox-Active Tris(amido) Ligand. J Am Chem Soc 2009, 131, 3307–3316. [PubMed: 19219982]
7. Bahnmüller S; Plotzitzka J; Baabe D; Cordes B; Menzel D; Schartz K; Schweyen P; Wicht R; Bröring M Hexaethyltripyrrindione (H_3Et_6tpd): A Non-Innocent Ligand Forming Stable Radical Complexes with Divalent Transition-Metal Ions. Eur J Inorg Chem 2016, 4761–4768.
8. Gautam R; Astashkin AV; Chang TM; Shearer J; Tomat E Interactions of Metal-Based and Ligand-Based Electronic Spins in Neutral Tripyrrindione π Dimers. Inorg Chem 2017, 56, 6755–6762. [PubMed: 28497967]
9. Wu T; Macmillan SN; Rajabimoghadam K; Siegler MA; Lancaster KM; Garcia-Bosch I Structure, Spectroscopy, and Reactivity of a Mononuclear Copper Hydroxide Complex in Three Molecular Oxidation States. J Am Chem Soc 2020, 142, 12265–12276. [PubMed: 32531159]
10. Lecarme L; Kochem A; Chiang L; Moutet J; Berthiol F; Philouze C; Leconte N; Storr T; Thomas F Electronic Structure and Reactivity of One-Electron-Oxidized Copper(II) Bis(phenolate)-Dipyrrin Complexes. Inorg Chem 2018, 57, 9708–9719. [PubMed: 29616807]
11. Kaim W Electron Transfer Reactivity of Organometallic Compounds Involving Radical-Forming Noninnocent Ligands. Proceedings of the National Academy of Sciences India Section A - Physical Sciences 2016, 86, 445–457.
12. Kaim W The Shrinking World of Innocent Ligands: Conventional and Non-Conventional Redox-Active Ligands. Eur J Inorg Chem 2012, 343–348.
13. Chaudhuri P; Nazari Verani C; Bill E; Bothe E; Weyhermüller T; Wieghardt K Electronic Structure of Bis(*o*-iminobenzosemiquinonato)metal Complexes (Cu, Ni, Pd). The Art of Establishing Physical Oxidation States in Transition-Metal Complexes Containing Radical Ligands. J Am Chem Soc 2001, 123, 2213–2223. [PubMed: 11456867]
14. Luca OR; Crabtree RH Redox-active ligands in catalysis. Chem Soc Rev 2013, 42, 1440–1459. [PubMed: 22975722]
15. Speier G; Csihony J; Whalen AM; Pierpont CG Studies on Aerobic Reactions of Ammonia/3,5-Di-*tert*-butylcatechol Schiff-Base Condensation Products with Copper, Copper(I), and Copper(II). Strong Copper(II)-Radical Ferromagnetic Exchange and Observations on a Unique N-N Coupling Reaction. Inorg Chem 1996, 35, 3519–3524.
16. Bill E; Müller J; Weyhermüller T; Wieghardt K Intramolecular Spin Interactions in Bis(phenoxyl)metal Complexes of Zinc(II) and Copper(II). Inorg Chem 1999, 38, 5795–5802.
17. Van Leest NP; De Zwart FJ; Zhou M; De Bruin B Controlling Radical-Type Single-Electron Elementary Steps in Catalysis with Redox-Active Ligands and Substrates. JACS Au 2021, 1, 1101–1115. [PubMed: 34467352]
18. Broere DLJ; Plessius R; van der Vlugt JI New avenues for ligand-mediated processes – expanding metal reactivity by the use of redox-active catechol, o-aminophenol and o-phenylenediamine ligands. Chem Soc Rev 2015, 44, 6886–6915. [PubMed: 26148803]
19. Kessler BJO; Mansoor IF; Wozniak DI; Emge TJ; Lipke MC Controlling Intramolecular and Intermolecular Electronic Coupling of Radical Ligands in a Series of Cobaltoviologen Complexes. J Am Chem Soc 2023, 145, 15924–15935. [PubMed: 37460450]
20. van der Vlugt JI Radical-Type Reactivity and Catalysis by Single-Electron Transfer to or from Redox-Active Ligands. Chemistry - A European Journal 2019, 25, 2651–2662.
21. Munhá RF; Zarkesh RA; Heyduk AF Tuning the Electronic and Steric Parameters of a Redox-Active Tris(amido) Ligand. Inorg Chem 2013, 52, 11244–11255. [PubMed: 24011392]
22. Barman SK; Jones JR; Sun C; Hill EA; Ziller JW; Borovik AS Regulating the Basicity of Metal-Oxido Complexes with a Single Hydrogen Bond and Its Effect on C-H Bond Cleavage. J Am Chem Soc 2019, 141, 11142–11150. [PubMed: 31274298]

23. Drummond MJ; Ford CL; Gray DL; Popescu CV; Fout AR Radical Rebound Hydroxylation Versus H-Atom Transfer in Non-Heme Iron(III)-Hydroxo Complexes: Reactivity and Structural Differentiation. J Am Chem Soc 2019, 141, 6639–6650. [PubMed: 30969766]
24. Shook RL; Borovik AS Role of the secondary coordination sphere in metal-mediated dioxygen activation. Inorg Chem 2010, 49, 3646–3660. [PubMed: 20380466]
25. Lee JL; Ross DL; Barman SK; Ziller JW; Borovik AS C-H Bond Cleavage by Bioinspired Nonheme Metal Complexes. Inorg Chem 2021, 60, 13759–13783. [PubMed: 34491738]
26. Borovik AS Role of metal–oxo complexes in the cleavage of C–H bonds. Chem Soc Rev 2011, 40, 1870–1874. [PubMed: 21365079]
27. Bhadra M; Lee JYC; Cowley RE; Kim S; Siegler MA; Solomon EI; Karlin KD Intramolecular Hydrogen Bonding Enhances Stability and Reactivity of Mononuclear Cupric Superoxide Complexes. J Am Chem Soc 2018, 140, 9042–9045. [PubMed: 29957998]
28. Sinha S; Das S; Sikari R; Parua S; Brandaõ P; Demeshko S; Meyer F; Paul ND Redox Noninnocent Azo-Aromatic Pincers and Their Iron Complexes. Isolation, Characterization, and Catalytic Alcohol Oxidation. Inorg Chem 2017, 56, 14084–14100. [PubMed: 29120616]
29. Balaghi SE; Safaei E; Chiang L; Wong EWY; Savard D; Clarke RM; Storr T Synthesis, characterization and catalytic activity of copper(II) complexes containing a redox-active benzoxazole iminosemiquinone ligand. Dalton Transactions 2013, 42, 6829–6839. [PubMed: 23487254]
30. Leipzig BK; Rees JA; Kowalska JK; Theisen RM; Kavčič M; Poon PCY; Kaminsky W; DeBeer S; Bill E; Kovacs JA How Do Ring Size and π-Donating Thiolate Ligands Affect Redox-Active, α-Imino-*N*-heterocycle Ligand Activation? Inorg Chem 2018, 57, 1935–1949. [PubMed: 29411979]
31. Costentin C; Savéant JM; Tard C Ligand “noninnocence” in coordination complexes vs. Kinetic, mechanistic, and selectivity issues in electrochemical catalysis. Proc Natl Acad Sci U S A 2018, 115, 9104–9109. [PubMed: 30143579]
32. Burns KT; Marks WR; Cheung PM; Seda T; Zakharov LN; Gilbertson JD Uncoupled Redox-Inactive Lewis Acids in the Secondary Coordination Sphere Entice Ligand-Based Nitrite Reduction. Inorg Chem 2018, 57, 9601–9610. [PubMed: 29608297]
33. Onderko EL; Silakov A; Yosca TH; Green MT Characterization of a selenocysteine-ligated P450 compound I reveals direct link between electron donation and reactivity. Nat Chem 2017, 9, 623–628. [PubMed: 28644466]
34. Benecky MJ; Frew JE; Scowen N; Jones P; Hoffman BM EPR and ENDOR Detection of Compound I from *Micrococcus lysodeikticus* Catalase. Biochemistry 1993, 32, 11929–11933. [PubMed: 8218266]
35. Cook SA; Bogart JA; Levi N; Weitz AC; Moore C; Rheingold AL; Ziller JW; Hendrich MP; Borovik AS Mononuclear complexes of a tridentate redox-active ligand with sulfonamido groups: Structure, properties, and reactivity. Chem Sci 2018, 9, 6540–6547. [PubMed: 30310585]
36. Brazzolotto D; Bogart JA; Ross DL; Ziller JW; Borovik AS Stabilizing a Ni^{II}-aqua complex via intramolecular hydrogen bonds: Synthesis, structure, and redox properties. Inorganica Chim Acta 2019, 495, 118960–118965. [PubMed: 31607758]
37. Yang L; Powell DR; Houser RP Structural variation in copper(I) complexes with pyridylmethylamide ligands: Structural analysis with a new four-coordinate geometry index, τ4. Journal of the Chemical Society. Dalton Transactions 2007, 955–964.
38. Gardner EJ; Cobb CR; Bertke JA; Warren TH Tris(pyrazolyl)borate Copper Hydroxide Complexes Featuring Tunable Intramolecular H-Bonding. Inorg Chem 2019, 58, 11248–11255. [PubMed: 31390193]
39. Jones JR; Ziller JW; Borovik AS Modulating the Primary and Secondary Coordination Spheres within a Series of Co^{II}-OH Complexes. Inorg Chem 2017, 56, 1112–1120. [PubMed: 28094522]
40. Wojtulewski S; Grabowski SJ Different donors and acceptors for intramolecular hydrogen bonds. Chem Phys Lett 2003, 378, 388–394.
41. Kunert R; Philouze C; Berthiol F; Jarjayes O; Storr T; Thomas F Distorted copper(II) radicals with sterically hindered salens: electronic structure and aerobic oxidation of alcohols. Dalton Transactions 2020, 49, 12990–13002. [PubMed: 32909589]

42. Hoffman BM; DeRose VJ; Doan PE; Gurbiel RJ; Houseman ALP; Telser J Metalloenzyme Active-Site Structure and Function through Multifrequency CW and Pulsed ENDOR. in EMR of Paramagnetic Molecules. Biological Magnetic Resonance (eds. Berliner LJ & Reuben J) (Springer, 1993). vol. 13 151–218.
43. Abragam A; Bleaney B Electron Paramagnetic Resonance of Transition Ions. (Clarendon P., 1970).
44. DuBois JL; Mukherjee P; Stack TDP; Hedman B; Solomon EI; Hodgson KO A systematic K-edge X-ray absorption spectroscopic study of Cu(III) sites. J Am Chem Soc 2000, 122, 5775–5787.
45. Tomson NC; Williams KD; Dai X; Sproules S; Debeer S; Warren TH; Wieghardt K Re-evaluating the Cu K pre-edge XAS transition in complexes with covalent metal-ligand interactions. Chem Sci 2015, 6, 2474–2487. [PubMed: 29308158]
46. Hitchman MA Interpretation of Copper(II) Hyperfine Parameters. Inorg Chem 1985, 24, 4762–4765.
47. Donoghue PJ; Tehranchi J; Cramer CJ; Sarangi R; Solomon EI; Tolman WB Rapid C-H Bond Activation by a Monocopper(III)-Hydroxide Complex. J Am Chem Soc 2011, 133, 17602–17605. [PubMed: 22004091]
48. Kanamori J Superexchange Interaction and Symmetry Properties of Electron Orbitals. J. Phys. Chem. Solids 1959, 10, 87–98.
49. Goodenough JB Theory of the Role of Covalence in the Perovskite-Type Manganites [La, M(II)]MnO_3. Physical Review 1955, 100, 564–573.
50. Goodenough JB Spin-Orbit-Coupling Effects in Transition-Metal Compounds. Physical Review 1968, 171, 466–479.
51. Bencini A; Gatteschi D Electron Paramagnetic Resonance of Exchange Coupled Systems. (Springer Berlin Heidelberg, 1990).
52. Okazawa A; Hashizume D; Ishida T Ferro-and antiferromagnetic coupling switch accompanied by twist deformation around the copper(II) and nitroxide coordination bond. J Am Chem Soc 2010, 132, 11516–11524. [PubMed: 20669955]

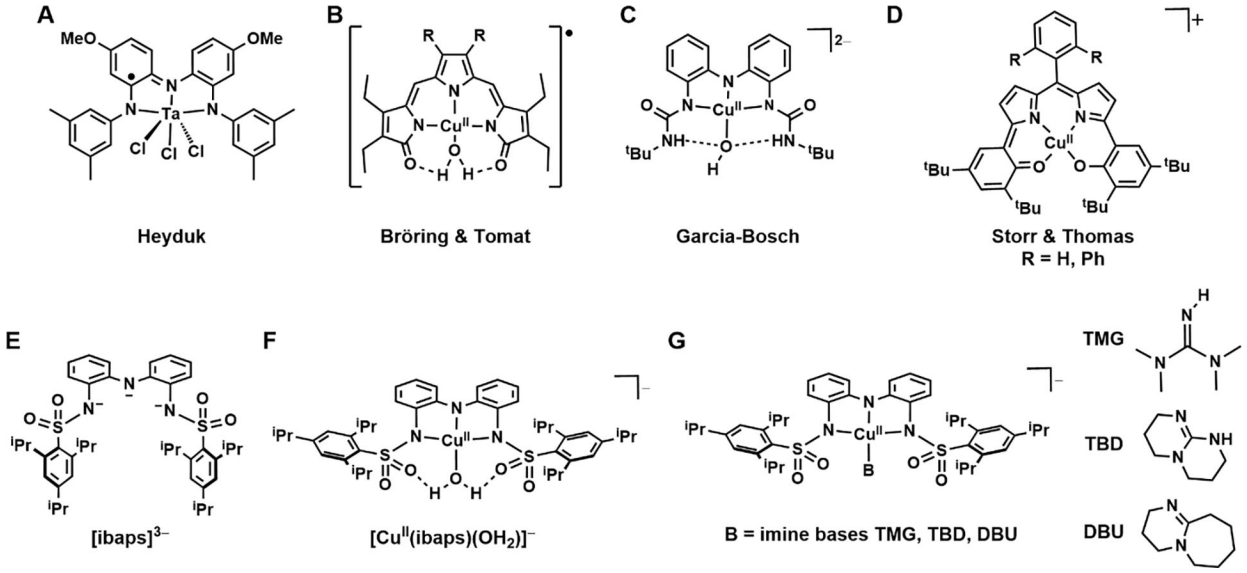

Figure 1.

Synthetic metal complexes from the literature (A-D); the redox-active ligand (E) and complexes used in this study (F,G).

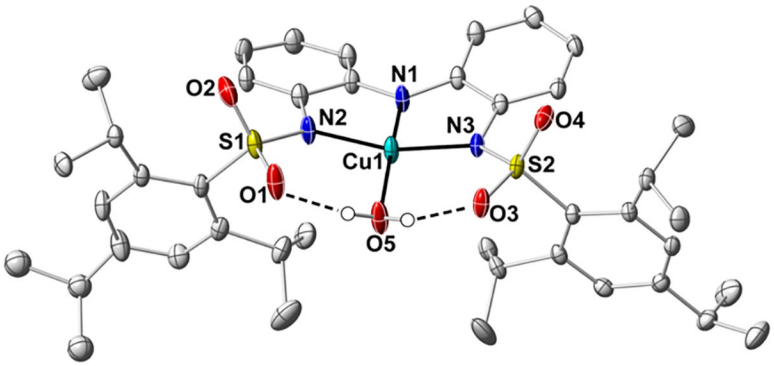

Figure 2.

Thermal ellipsoid diagram depicting the molecular structure of **1**-OH_2 (CCDC Code: 2291042). The thermal ellipsoids are drawn at the 50 % probability level, and implicit hydrogen atoms and the TBA cation are removed for clarity.

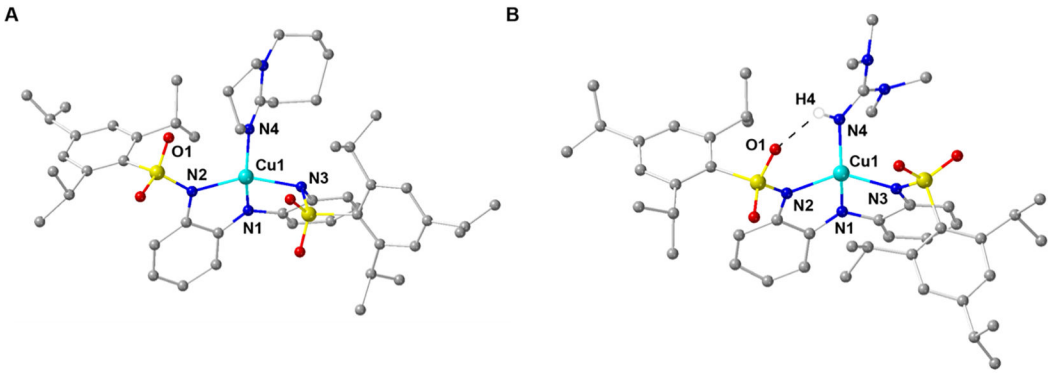

Figure 3.

Ball and stick depictions of the molecular structures for **1**-DBU and **2**-TMG (CDCC Codes: 2291043 and 2291041). The counterion and hydrogen atoms are removed for clarity with the exception of the hydrogen atom in **2**-TMG that is involved in an H-bond. Selected bond angles (°) for **1**-DBU (**2**-TMG): N1-Cu1-N4, 159.3(3) (148.5(2)); N2-Cu1-N3, 154.6(2) (142.8(2)).

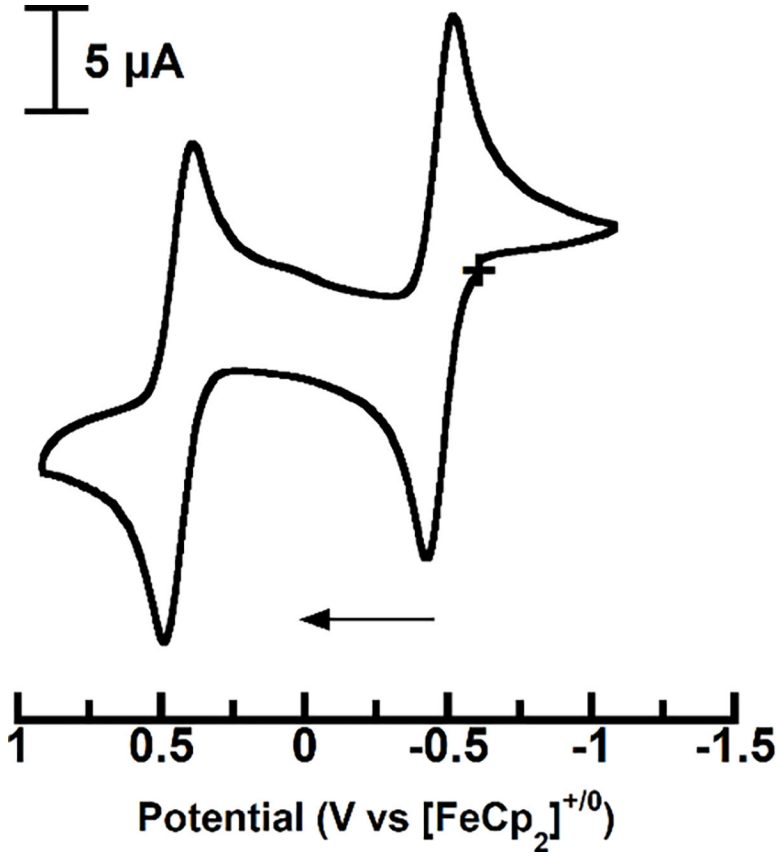

Figure 4.
Cyclic voltammogram of **1**-OH_2 at room temperature in DCM.

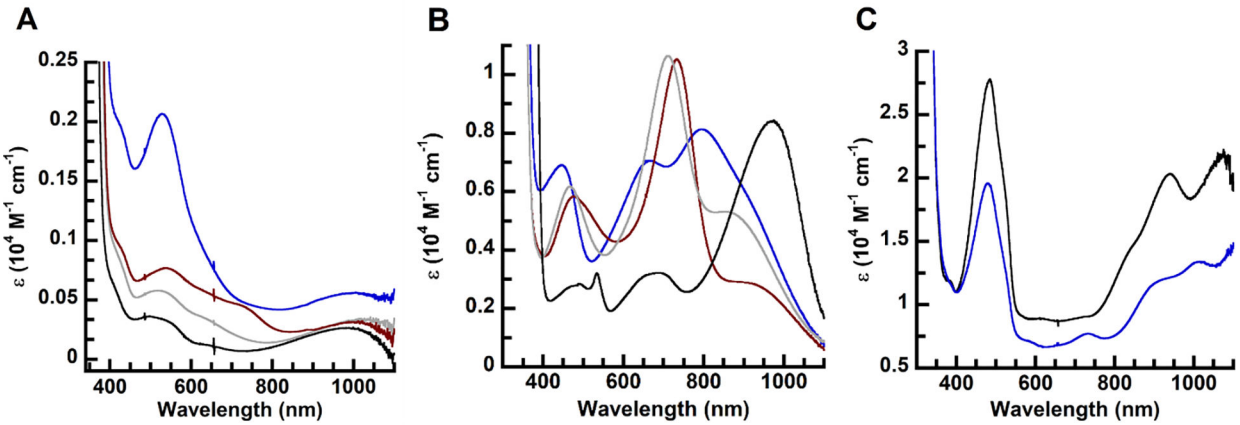

Figure 5.

Electronic absorbance spectra of the (A) **1**-L species and (B) **2**-L species in 1:1 DCM:THF at 22 °C and (C) the **3**-L species in neat DCM at −80 °C. L= aqua (black), DBU (gray), TMG (blue), and TBD (red).

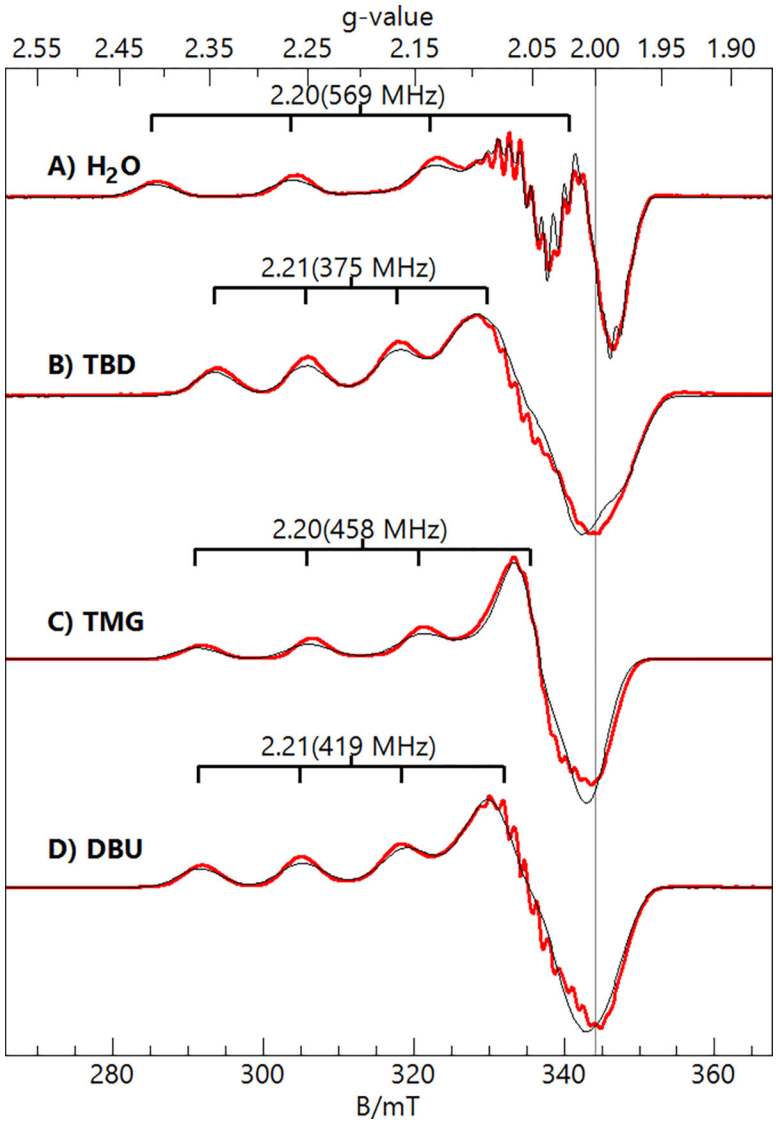

Figure 6.

X-band (9.64 GHz, 0.2 mW) EPR spectra (red traces) and simulations (black traces) of the **1**-L complexes in DCM:THF. The simulation parameters are listed in Table 3. Sample temperature, 12 K.

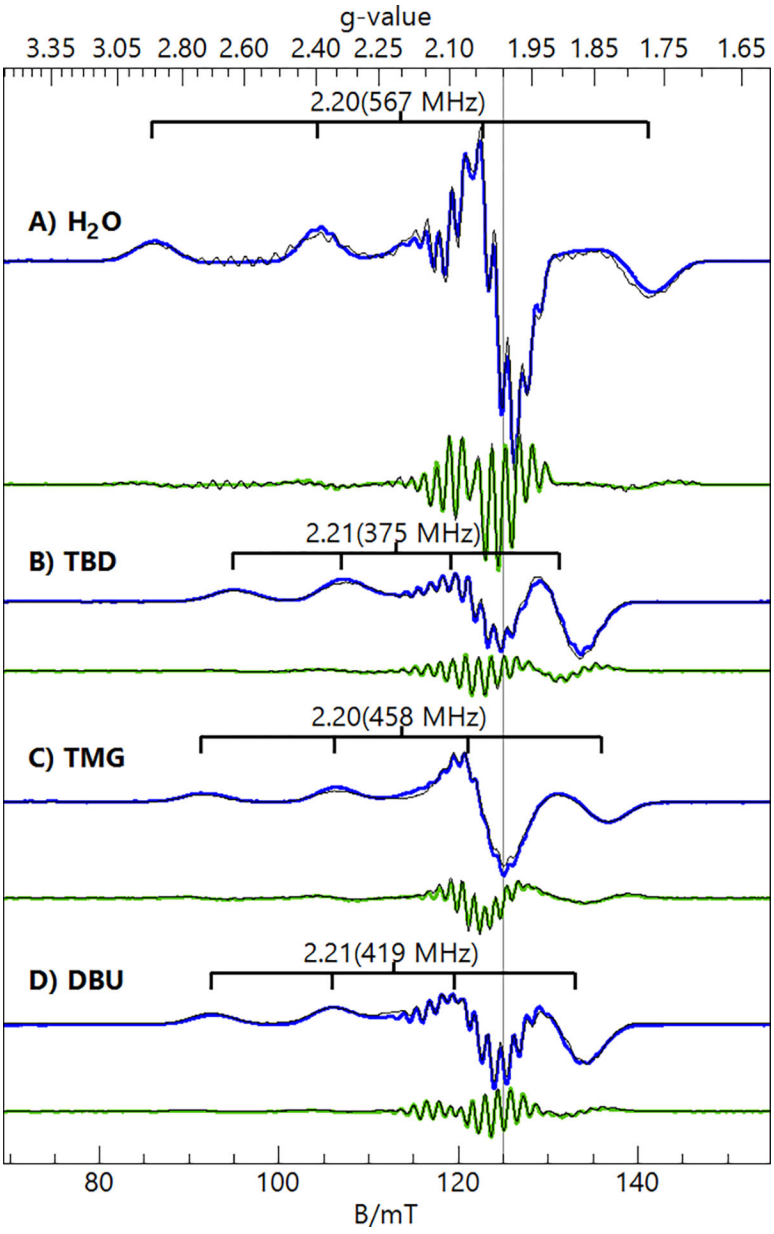

Figure 7.

S-band (3.50 GHz, 0.03 mW) EPR spectra (1st derivative, blue traces; 2nd derivative, green traces) and simulations (black traces) of the **1**-L complexes in DCM:THF. The simulation parameters are listed in Table 3. Sample temperature, 30 K.

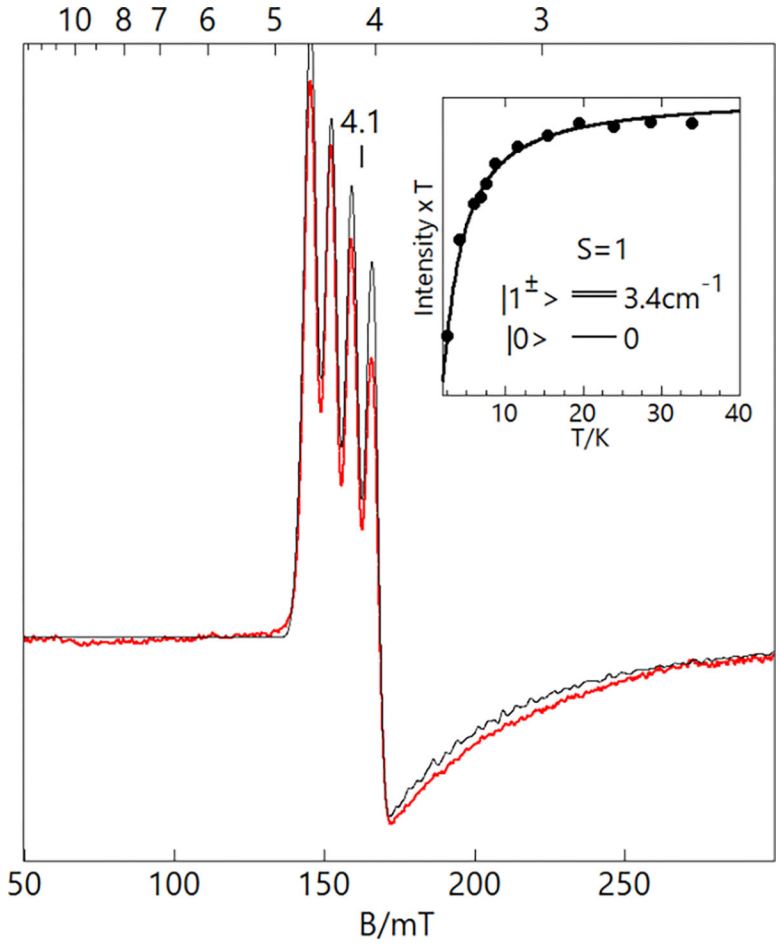

Figure 8.

Parallel-mode X-band (9.337 GHz) EPR spectrum (red trace) of **2**-OH_2, 12 mM in DCM:THF. The simulation (black trace) uses the parameters listed in Table 3 and is quantitative for the sample concentration. Sample temperature: 6 K, microwave power: 2 mW. The inset shows the temperature dependence of the signal, plotted as signal intensity × temperature (•) versus temperature. The curve is calculated from the spin Hamiltonian for $S = 1$ and $D = +3.4\ cm^{-1}$.

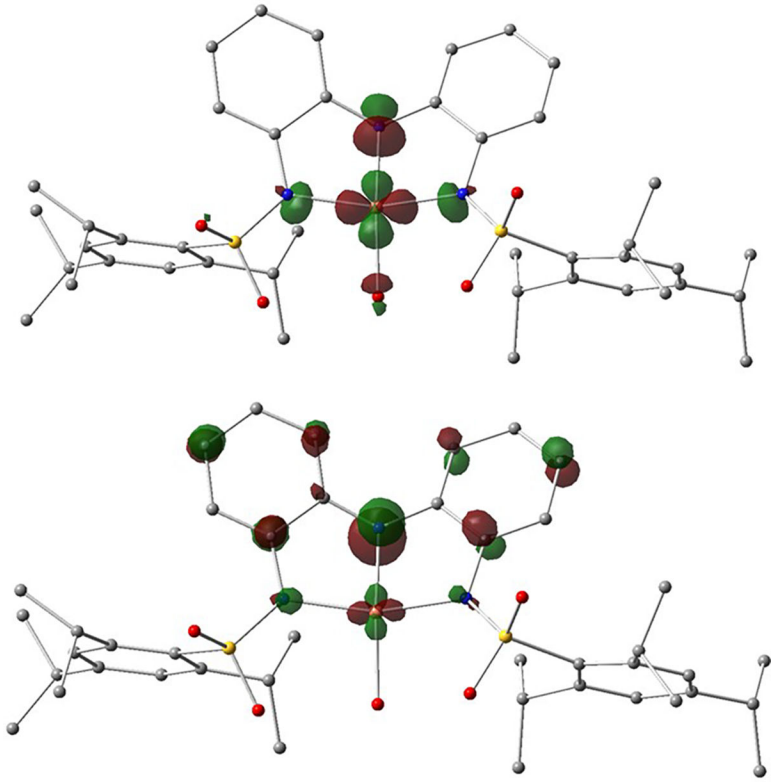

Figure 9.

Molecular orbitals of **1**-OH_2 containing the unpaired electron (top, primarily $d_{x^2-y^2}$) and the redox-active HOMO (bottom, primarily p_z of the central N atom).

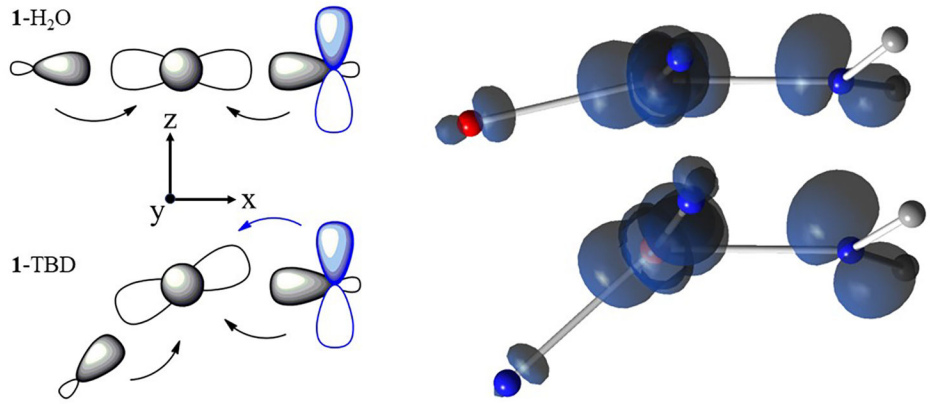

Figure 10.

Left: Orbital interactions between $x^2 - y^2$ and the ligand/N1 atom of $[ibaps]^{3-}$. The component of the redox-active π orbital at N1 is shown in blue. Right: corresponding spin densities from DFT showing spin populations in Cu $x^2 - y^2$ and sp^2 and p_z orbitals of N1, the latter arising from the transfer of minority β spin density into the $x^2 - y^2$ orbital. For clarity, only the Cu center, its coordinating atoms, and the C atoms of $[ibaps]^{3-}$ are displayed.

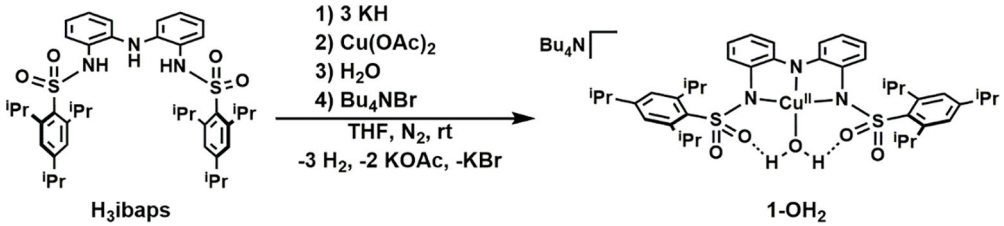

Scheme 1.

Synthetic route for the preparation of **1**-OH_2.

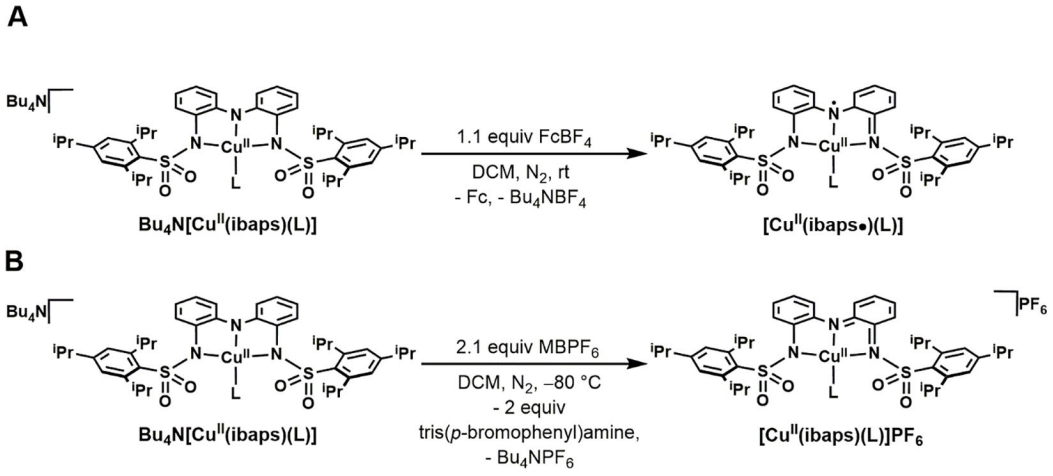

Scheme 2.

Preparative routes of **2**-L (**A**) and **3**-L (**B**) complexes.

Table 1.

Selected Metrical Parameters for **1**-OH_2

Bond Distances (Å) and Angles (°)	
Cu1-N1	1.874(1)
Cu1-N2	1.993(1)
Cu1-N3	2.000(1)
Cu1-O1	1.960(1)
O1…O5	2.624(1)
O3…O5	2.610(1)
N1-Cu1-O5	166.01(6)
N2-Cu1-N3	163.48(6)

Table 2.

Redox Properties of **1**-L in DCM and relevant literature values.[a]

Complex	$E_{1/2}$	$E_{1/2}'$
I-OH2	−0.48	+0.44
1-TBD	−0.70	+0.51[b]
1TMG	−0.75	+0.41
1-DBU	−0.71	+0.55[b]
$[Cu(TD1\bullet)(H_2O)]$[c]	~ −0.6	−0.052
$^{tBu}CuOH$[d]	−1.05	−0.28

[a] V versus $[Fe^{III/II}Cp2]^{+/0}$ observed at 100 mV/s where L = H_2O, TBD, DBU, or TMG;

[b] E_{pa};

[c] ref 8, in CH_3CN;

[d] ref 9, in DMF.

Table 3.

Select Spectroscopic Properties of the **1**-L, **2**-L, and **3**-L Complexes.

Complex	λ_{max}/nm (e_M/M^{-1} cm^{-1})	g-value(s)[b]	A_{Cu} (MHz)[a,b]	A_N [b,d] (MHz)	ν(OH or NH) (cm^{-1})[c]	ν(OD or ND) (cm^{-1})[c]
1-OH_2	316 (24000), 341 (30000), 500 (360), 540 (330), 990 (260)[f]	2.03, 2.06, 2.20	−50, −50, −570 (−220)[a]	39, 44	3180	2424
1-TBD	316 (20000), 340 (25000), 430 (sh), 545 (900), 730 (680), 995 (390)[f]	2.04, 2.05, 2.21	−175, 40, −375 (−170)	41, 35	3300	2480
1-TMG	347 (29000), 340 (25000), 425 (2100), 525 (2100), 1000 (700)[f]	2.04, 2.06, 2.20	−10, −20, −460 (−160)	40, 29	3330	2480
1-DBU	317 (23000), 340 (29000), 488 (500), 550 (600), 697 (320), 990 (300)[f]	2.03, 2.06, 2.21	−110, 55, −420 (−160)	41, 35	NA	NA
2-OH_2	346 (20000), 380 (16000), 480 (2800), 532 (3300), 685 (3300), 965 (8400)[f]	4.1[e]	195[e]	NA	3225	2424
2-TBD	343 (21000), 472 (5200), 731(10000), 910sh (2700)[f]	NA	NA	NA	3330	2480
2-TMG	342 (26000), 450 (6900), 665 (7100), 795 (8100), 920 (5600)[f]	NA	NA	NA	3360	2490
2-DBU	341 (24000), 472 (6100), 718 (10600), 865 (5300)[f]	NA	NA	NA	NA	NA
3-OH_2	387 (12000), 485 (28000), 530sh (17000), 610 (8900), 726 (9100), 840sh (14000), 938 (20000), 1075 (22000)g	2.04, 2.08, 2.26	−45, −30, −480 (−185)	37, 36	NA	NA
3-TMG	479 (20000), 525sh (13000), 582sh (7100), 735 (7700), 920 (12000), 1010 (13000), >1100 (~15000)[g]	2.02, 2.06, 2.22	0, 0, −410 (−140)	-	NA	NA

[a] (A_{iso}).

[b] In DCM:THF.

[c] In solid-state.

[d] Isotropic values of the 2 (**1**-OH_2) or 3 equivalent ^{14}N atoms, the second value is for the lone inequivalent ^{14}N atom.

[e] Observed z-component values from $S = 1$.

[f] In DCM:THF at 22 °C

[g] In neat DCM at −80

Table 4.

Selected Bond Lengths (Å) and Angles (°) for **1**-L calculated from DFT

L	Cu-N1	Cu-O1/N	Cu-N2/N3	N1-Cu-O5/N	N2-Cu-N3
H_2O	1.915	2.019	2.030/2.045	166	162
TMG	1.945	1.996	2.098/2.108	156	148
TBD	1.974	2.032	2.110/2.076	137	146
DBU	1.966	2.043	2.108/2.114	147	147

[a] see Figures 2 and 3 for atomic numbering

Table 5.

DFT-calculated X-Cu-N1 bond angles and relative energies for the $[Cu(ibaps)L]^n$ and $[Cu(ibaps^T)X]^n$ complexes.[a]

Complex	1-L	2-L (broken symmetry)	2-L (ferromagnetic)	ΔE[c]	3-L
$[Cu(ibaps)OH_2]^n$	166	171	172	−450	172
$[Cu(ibaps^T)OH_2]^n$	131[d]	137	180	370	176
$[Cu(ibaps)TMG]^n$	156	153	162	830	158
$[Cu(ibaps)DBU]^n$	147	143	165	560	149
$[Cu(ibaps^T)DBU]^n$	159	152	180	532	179
$[Cu(ibaps)TBD]^n$	137	144	152	1070	152
$[Cu(ibaps^T)TBD]n$,[b]	123	140	175	581	179
$[Cu(ibaps^T)N(H)CH_2]n$,[b]	156	141	180	800	178
$[Cu(ibaps^T)NH_3]^n$	156	145	178	491	175

[a] T is truncated ligand with the sulfonamido aryl groups replaced by hydrogen atoms. Angles in degrees. Broken symmetry refers to antiparallel spins, and ferromagnetic refers to complexes with the $S = 1$ spin ground state. For selected computed bond lengths in **1**-X and **2**-X (X = OH_2 and DBU) see Table S10.

[b] During optimization, the imine and TBD plane was kept orthogonal to the ibaps plane by imposing suitable dihedral constraints (see Supporting Information).

[c] Difference in the energies of the ferromagnetic and the broken symmetry states, $E_{rerro} - E_{Broken\ Symm}$, in wavenumbers.

[d] In this optimization, one of the lone pairs of the water ligand was directed toward the Cu throughout the optimization by imposing suitable angular and dihedral constraints (see Supporting Information).

Table 6.

Comparison of experimental and DFT-calculated A_z^{SD} values (in MHz) for select $[Cu(ibaps)L]^n$ complexes.

Complexes	A_z^{SD}, experimental	A_z^{SD}, DFT
1-OH_2	−470	−460
1-TMG	−420	−390
1-TBD	−330	−350
1-DBU	−350	−350
3-OH_2	−500	−500
3-TMG	−450	−460